PCCP

ROYAL SOCIETY OF CHEMISTRY

PAPER

View Article Online
View Journal | View Issue

Cite this: *Phys. Chem. Chem. Phys.*, 2024, **26**, 26037

Fundamental data for modeling electron-induced processes in plasma remediation of perfluoroalkyl substances†

Marin Sapunar, [a] Mackenzie Meyer, [b] Harindranath B. Ambalampitiya, [c] Mark J. Kushner [b] and Zdeněk Mašín [d]*

Received 7th May 2024,
Accepted 26th September 2024

DOI: 10.1039/d4cp01911c

rsc.li/pccp

Plasma treatment of per- and polyfluoroalkyl substances (PFAS) contaminated water is a potentially energy efficient remediation method. In this treatment, an atmospheric pressure plasma interacts with surface-resident PFAS molecules. Developing a reaction mechanism and modeling of plasma–PFAS interactions requires fundamental data for electron–molecule reactions. In this paper, we present results of electron scattering calculations, potential energy landscapes and their implications for plasma modelling of a dielectric barrier discharge in PFAS contaminated gases, a first step towards modelling of plasma–water–PFAS intereactions. It is found that the plasma degradation of PFAS is dominated by dissociative electron attachment with the importance of other contributing processes varying depending on the molecule. All molecules posses a large number of shape resonances – transient negative ion states – from near-threshold up to ionization threshold. These states lie in the region of the most probable electron energies in the plasma (4–5 eV) and consequently are expected to further enhance the fragmentation dynamics in both dissociative attachment and dissociative excitation.

1 Introduction

Per- and polyfluoroalkyl substances (PFAS) are a classification of molecules commonly used in industrial applications.[1] Due to the strong C–F bond, these compounds do not naturally degrade. Recent concern over their accumulation in drinking water has led to increased regulation of their concentrations. The European Chemicals Agency (ECHA) limits total PFAS concentration to 0.5 μg L^{-1}.[2] The United States Environmental Protection Agency (EPA) has proposed maximum contaminant levels of 4 ppt for two common PFAS molecules, PFOA and PFOS, and has proposed restricting PFBS concentration in conjunction with other PFAS molecules.[3] Recent research has focused on remediation methods that break apart the PFAS molecule.[4] Processes that aim to mineralize PFAS molecules include sonolysis and atmospheric pressure plasma exposure. In atmospheric pressure plasma exposure, degradation of PFAS in water occurs in reactions with gas-phase reactive species, including electrons, ions, and excited states of the feedstock gas, as well as reactive species present in the liquid, including solvated electrons.[5,6] However, much of the fundamental data, particularly around electron impact collisions in the gas phase, is not available. In this work, we report electron impact dissociative excitation cross sections relevant for plasma exposure. We focus on four PFAS molecules: perfluorobutanoic acid (PFBA), perfluorooctanoic acid (PFOA), perfluorobutanesulfonic acid (PFBS) and perfluorooctanesulfonic acid (PFOS). The molecules studied are shown in Fig. 1.

The mechanism of both PFOA and PFOS degradation through photochemical treatment is attributed to reactions initiated by the solvated electron (e_{aq}^-).[7] The same species was also shown to be crucial for plasma treatment in liquid discharge reactors.[6] However, the same study concluded that the primary step of the degradation is likely different in gas phase discharge reactors due to the possibility of interaction between free electrons or argon ions with PFAS molecules adsorbed at the gas–water interface. Wiens *et al.*[8] studied the plasma degradation mechanism of these molecules in the gas phase to avoid the complications introduced by the solvent or gas–liquid interface environment on the molecules. Through their experiments, they quantified the charged products of

[a] *Division of Physical Chemistry, Ruđer Bošković Institute, Bijenička cesta 54, 10000 Zagreb, Croatia*
[b] *Department of Electrical Engineering and Computer Science, University of Michigan, Ann Arbor, MI 48109, USA. E-mail: maemeyer@umich.edu, mjkush@umich.edu*
[c] *Quantemol Ltd, 320 City Rd, London EC1V 2NZ, UK*
[d] *Faculty of Mathematics and Physics, Charles University, Institute of Theoretical Physics, V Holešovičkách 2, 18000 Prague, Czech Republic. E-mail: zdenek.masin@matfyz.cuni.cz*

† Electronic supplementary information (ESI) available. See DOI: https://doi.org/10.1039/d4cp01911c

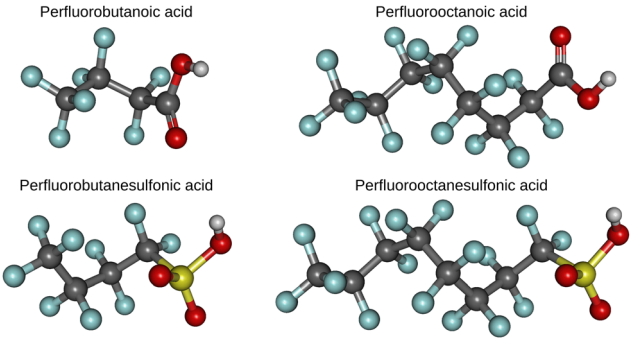

Fig. 1 The molecules studied in this work. Top row from left to right: PFBA, PFOA. Bottom row from left to right: PFBS, PFOS.

PFBA (and, to a lesser extent, PFOA and PFOS) formed through reactions with Ar^+ and dissociative electron attachment, but could not track neutral fragments formed.

The energy of electrons involved in plasma degradation processes is more than sufficient to electronically excite these molecules, but no studies of their excited state chemistry have been performed thus far. Here we perform the first step in understanding the excited state processes leading to degradation of these compounds by (1) identifying the likely initial states to which these molecules are excited through UV absorption or through inelastic scattering of low-energy electrons and (2) a systematic study of the excited state potential energy surfaces (PES) of these compounds to identify bonds where the initial steps of the degradation reaction can occur. The focus on pairs of molecules with the same functional group and different lengths of the carbon chain allows us to determine the effect of the chain length on the excited state chemistry of the molecules.

Neither experimental nor calculated electron collision data for the large polyfluoroalakyl molecules is available. For theory, the size of the molecules (both spatial and in terms of the number of electrons) presents a formidable challenge. We meet this challenge by employing our recently developed Born approach[9] suitable for calculating optically-allowed transitions over a wide energy range. Additionally, due to the presence of strongly electronegative atoms and unoccupied virtual orbitals we can expect formation of a number of elastic and inelastic scattering resonances. Those transient negative ion states strongly influence internal dynamics of the molecule, including breakup. For that reason, characterization of resonances is key to understanding the electron attachment process. To characterize the resonances and to calculate cross sections for the optically-forbidden transitions in the low-energy region we use the *ab initio R*-matrix method for electron collisions with molecules[10] and our recently developed method for direct localization of scattering resonances.[11] To the best of our knowledge PFOS is one of the largest molecules for which an *ab initio* electron scattering calculation was attempted. Consequently, our calculations are limited to the simplest elastic scattering model and a very simple inelastic model. These models are designed to provide well-defined approximations to future accurate models and to reveal the number and basic parameters of the scattering resonances.

Many studies have investigated degradation of PFAS compounds in water due to atmospheric pressure plasma exposure.[6,12–17] However, to our knowledge, no modelling of the plasma treatment of PFAS contaminated water has occurred as the complex chemistry occurring between the PFAS molecules and plasma-produced reactive species (in particular, electrons) poses a challenge for modelling studies. Using the recommended electron impact cross sections calculated in this work, we aim to provide a first step towards the modelling of PFAS contaminated water. To that end, the 0D plasma chemistry model *GlobalKin* is used to examine the decomposition in an Ar/PFAS system. As a first step, the chemistry is limited to gas phase reactions.

In Section 2 we outline the theoretical methods and the parameters used in the calculation. This is followed in Section 3 by results for the fragmentation pathways of all molecules and by results of the electron scattering calculations in both the Born approximation and using the *R*-matrix approach. In Section 3.6 the electron impact data are combined with a comprehensive modelling of plasma degradation of PFAS molecules in Ar, followed by discussion of the role of the individual processes in Section 4 and Conclusions in Section 5.

2 Theoretical methods

2.1 Electronic structure calculations

The ground state minima of all four molecules have been optimized at the MP2/cc-pVDZ level. For excited state calculations, several electronic structure methods and basis set combinations have been attempted and ADC(2)/aug-cc-pVDZ has been found to offer a good balance of efficiency and accuracy. Reasonably accurate excitation energies were obtained already using time-dependent density functional theory with the Tamm–Dancoff approximation (TDA) approximation at the TDA/PBE0/def2-SVPD level, but the potential energy surfaces (PESs) calculated using this method exhibited qualitatively wrong behaviour along key pathways. Multireference calculations were also performed at the CASSCF and CASPT2 level. Diffuse functions in the basis set were needed to accurately describe a significant number of states in all four molecules, but increasing the basis set beyond double-ζ did not have a large effect on the accuracy of the calculations. All DFT and ADC(2) calculations were performed using the Turbomole program package.[18,19] Complete active space calculations were performed using the Molpro[20] and BAGEL[21] packages.

Cuts along all likely dissociation pathways on the PESs of the molecules were studied. Geometries along the cuts were obtained through constrained optimisations of the S_0 state at the PBE0/def2-SVPD level and (for the most likely channels of PFBA) of the S_1 and T_1 surfaces at the ADC(2)/aug-cc-pVDZ level with constraints on the bond being extended and the C–O–H angle in the case of hydrogen dissociation curves (to prevent the hydrogen jumping to other oxygen atoms). A low convergence

threshold was used for the optimisations to reduce computational time. Single point calculations along all scans were performed at the ADC(2)/aug-cc-pVDZ level. The method employed here is a single-reference method and is thus unable to accurately describe dissociation curves. However, the results should be accurate for distances large enough to estimate the relative feasibility of the various pathways.

2.2 Scattering calculations

2.2.1 *R*-Matrix calculations. The calculations were performed with UKRmol+ suite[10] with fixed nuclei which is an implementation of the molecular *R*-matrix approach, see ibid. The method uses division of space by a sphere enclosing the charge density of the target molecule to solve the Schrödinger equation inside and outside of the sphere separately. Inside the sphere it uses configuration–interaction techniques of quantum chemistry modified to include orbitals describing the unbound electron. The outer part of the wavefunction is treated as a one-electron problem for the unbound electron and both wavefunctions are matched on the sphere by the *R*-matrix. The calculations were performed for the optimized equilibrium geometries. Hartree–Fock and CASSCF orbitals were obtained with Molpro.[20]

The target electrons were described with the cc-pVDZ atomic basis set while the unbound electron was described using Gaussian-only continuum bases[22] centered on the center of mass with angular momenta up to $l_{max} = 6$. The *R*-matrix radius was 15 bohr with exception of the PFOS molecule for which we used radius of 18 bohr and a continuum basis with $l_{max} = 4$. The molecular integrals were computed in quad precision which prevents linear dependency issues between the target and continuum Gaussians and allowed us to retain all functions in the continuum basis.

To the best of our knowledge the PFOS molecule is the largest molecule treated by the *R*-matrix method so far which goes with the corresponding computational demands: the largest part of the calculation was the computation of the molecular integrals. The rest of the calculation was computationally simple due to the choice of small scattering models.

Two types of scattering models were employed: elastic static-exchange (SE model) and inelastic close-coupling with CASSCF target wavefunctions (CAS model). The static-exchange (SE) scattering model[10] employs Hartree–Fock orbitals and doesn't include any effects of electron correlation beyond the exchange interaction of all electrons in the system. The L^2 functions for the SE model have the form of the Hartree–Fock ground state coupled to virtual orbitals. In this case all available virtual orbitals were used. In case of the CAS models we included the standard set of configurations of this model:[10]

$$(\text{core})^{N_c} \quad \text{CAS}^{N_{as}}(\text{cont})^1$$

$$(\text{core})^{N_c} \quad \text{CAS}^{(N_{as}+1)}$$

Here N_c is the number of electrons in doubly occupied orbitals, N_{as} the number of active electrons, CAS stands for orbitals of the active space and "cont" for the continuum orbitals. To aid the description of the many shape resonances and to partially top up continuum angular momentum expansion in the inner region the set of "cont" orbitals included all virtual orbitals outside of CAS and the true continuum orbitals obtained by the standard procedure of orthogonalization of the primitive continuum functions against the set of all target orbitals.

For all molecules, except for PFOS, we included in the calculation all molecular orbitals generated by the atomic basis. In case of PFOS we included, due to computational limitations, only a subset of 355 instead of the full set of 455 molecular orbitals.

2.2.2 Born calculations for inelastic cross sections. Cross sections for the inelastic scattering for excitations into the 20 lowest singlet excited states at the ADC(2)/aug-cc-pVDZ level were calculated using the Born approximation using the implementation described previously.[9] Excitations of optically-forbidden (singlet–triplet) transitions cannot be calculated with our current Born implementation due to our approximation to neglect exchange interaction between the target and the unbound electron. Instead, for the triplets we relied solely on the *R*-matrix calculation. Integrated Born cross sections were evaluated based on a grid of 30 scattering angles and a small Lebedev quadrature containing 14 points was used for orientational averaging.

3 Results

3.1 Electronic structure calculations

Excitation energies of the 10 lowest singlet and 10 lowest triplet excited states of PFBA and PFOA and of PFBS and PFOS are given in Tables 1 and 2, respectively. Regardless of the chosen method, the lowest excited electronic states of pairs of molecules with the same functional group have very similar character and energies so here we will only comment in detail on the smaller molecules. The hole and particle natural transition orbitals (NTOs) with the largest contribution to the lowest excited states of PFBA and PFOA are shown in S_1 and S_2. The lowest state (S_1) of PFBA is an $n\pi^*$ transition approximately 2 eV below the next pair of states of nRyd(s) and a $\pi\pi^*$ character. The S_1 state is almost completely dark, with an oscillator strength two orders of magnitude smaller than that of the $\pi\pi^*$ state which would be the primary state excited by UV radiation. There is a degree of mixing between the S_3 ($\pi\pi^*$) and S_2 (nRyd(s)) states which results in the usually dark nRyd(s) having a non-negligible oscillator strength. The S_4 state at the ADC(2)/aug-cc-pVDZ level is a $\sigma\pi^*$ transition, followed by a πRyd(s) (S_5) state and a set of transitions (S_6–S_7) to 3p Rydberg orbitals. The qualitative description of these states remains at the TDA/PBE0/def2-SVPD level, however the $\sigma\pi^*$ states are stabilized with respect to ADC(2) and appear as the S_2 and S_5 states.

At the CASSCF level, the lowest lying states are well described by an active space of 8 electrons in 8 orbitals (8,8) and the aug-cc-pVDZ basis set. In terms of the orbital composition, the only noticeable difference is the σ orbital which is the

Table 1 Excitation energies for the ten lowest singlet and triplet transitions of PFBA and PFOA. The calculations were performed at the RI-ADC(2)/aug-cc-pVDZ, TDA/RI-PBE0/def2-SVPD, and CASSCF/cc-pVDZ levels. The values for the latter are only for those excited states included in the state averaging procedure

	PFBA			PFOA		
	ADC(2)	PBE0	CASSCF	ADC(2)	PBE0	CASSCF
S_1	5.48	5.46	6.48	5.34	5.45	5.33
S_2	7.40	7.81	9.14	7.44	7.83	9.24
S_3	8.00	7.96	9.39	7.92	7.91	10.02
S_4	8.55	8.58	10.86	8.53	8.16	10.83
S_5	8.58	8.78	11.28	8.59	8.31	10.92
S_6	9.20	8.86	12.79	8.61	8.40	12.53
S_7	9.28	9.02	13.09	8.99	8.69	12.76
S_8	9.33	9.29		9.22	8.82	
S_9	9.57	9.55		9.42	8.98	
S_{10}	9.72	9.63		9.49	9.08	
T_1	5.02	4.86	6.12	5.00	4.85	5.00
T_2	6.06	5.61	6.50	6.05	5.60	5.75
T_3	7.45	7.36	8.90	7.45	7.40	9.20
T_4	8.13	7.90	9.81	8.14	7.82	9.37
T_5	8.40	8.26	10.36	8.39	8.04	10.72
T_6	8.59	8.40	10.79	8.41	8.12	10.81
T_7	9.07	8.69	12.65	8.88	8.27	12.39
T_8	9.16	8.74	14.62	9.00	8.49	14.05
T_9	9.43	9.09		9.11	8.58	
T_{10}	9.47	9.22		9.21	8.68	

Table 2 Excitation energies for the ten lowest singlet and triplet transitions of PFBS and PFOS. The calculations were performed at the RI-ADC(2)/aug-cc-pVDZ, TDA/RI-PBE0/def2-SVPD, and CASSCF/cc-pVDZ levels. The values for the latter are only for those excited states included in the state averaging procedure

	PFBS			PFOS		
	ADC(2)	PBE0	CASSCF	ADC(2)	PBE0	CASSCF
S_1	7.58	7.74	8.58	7.57	7.76	8.41
S_2	7.78	7.86	8.95	7.77	7.87	8.88
S_3	8.04	8.23	9.16	8.02	8.21	9.18
S_4	8.24	8.39	9.70	8.21	8.35	9.22
S_5	8.32	8.45	10.09	8.30	8.42	9.65
S_6	8.49	8.57	10.45	8.48	8.55	9.80
S_7	8.58	8.63	11.05	8.55	8.61	10.48
S_8	8.60	8.66		8.58	8.64	11.39
S_9	8.76	8.79		8.71	8.74	
S_{10}	8.99	8.87		8.95	8.75	
T_1	7.19	7.11	8.23	7.16	7.09	8.22
T_2	7.43	7.39	8.57	7.42	7.39	8.44
T_3	7.62	7.61	8.67	7.60	7.59	8.63
T_4	7.77	7.66	8.91	7.76	7.64	8.82
T_5	7.91	7.81	9.02	7.89	7.80	8.91
T_6	8.02	7.92	9.25	8.01	7.91	9.06
T_7	8.16	7.97	9.40	8.15	7.93	9.09
T_8	8.39	8.22	10.13	8.37	8.18	9.68
T_9	8.45	8.26		8.42	8.24	9.80
T_{10}	8.52	8.35		8.50	8.33	

dominant contribution to the S_3 state at the CASSCF level and is significantly more delocalized in the S_4 state at the ADC(2) level. Without the diffuse basis functions, at the CASSCF(8,8)/cc-pVDZ level 3p Rydberg type orbitals are not sufficiently described by the basis set so only the five lowest states are accurately described. Comparing the energies of the states at the ADC(2), CASSCF and CASPT2 levels of theory, we see that CASSCF(8,8)/aug-cc-pVDZ (Table S1, ESI†) offers surprisingly accurate excitation energies which are only marginally improved by CASPT2. On the other hand, energies computed at the CASSCF(8,8)/cc-pVDZ level are significantly higher and are improved substantially by including the dynamical correlation with CASPT2.

Turning next to the sulfonic acids, the hole and particle NTOs with the largest contribution to the lowest excited states of PFBS and PFOS are shown in S_3 and S_4. The sulfo group, unlike the carboxyl group, does not contain any π orbitals and thus, no low-lying bright states. Instead, starting from approximately 7.5 eV, PFBS and PFOS exhibit a dense manifold of nσ* and nRyd transitions, all of which have oscillator strengths an order of magnitude or more lower than the bright ππ* state of PFBA. The σ* orbital which is the particle orbital for the three lowest transitions exhibits nodes on both the C–S and S–OH bonds indicating that these bonds are the most easily broken. At the CASSCF level, we see that the nσ* and the nRyd(s) states are qualitatively correct even when using the smaller (cc-pVDZ) basis set and a smaller active space of 10 electrons in 8 orbitals (Table S2 and Fig. S5, ESI†). This basis set is not adequate to describe states involving 3p Rydberg orbitals.

The CASSCF representation is accessible in the molecular *R*-matrix codes and we have used it in inelastic electron scattering models to complement the data calculated using the Born approach. Cross sections for impact excitation of both singlet and triplet states were calculated. Most importantly, *R*-matrix calculations produce a structured continuum including the presence of resonances which strongly affects all types of cross sections. Despite the drawbacks of using the more compact basis set for the description of the excited states of the target molecule, the *R*-matrix calculations were performed only with the cc-pVDZ basis due to the computational demands that would be required for the diffuse basis calculations: a larger *R*-matrix sphere and consequently a larger basis of continuum functions. While calculations for highly diffuse targets have been made in the past for small molecules and would be in principle possible even for the present targets using a mixed B-spline/Gaussian basis,[10] the number of the continuum functions required implies hugely expensive integral calculations: the limited benefit of the diffuse target basis doesn't justify such effort, see Section 3.3 for details.

3.2 Potential energy surface

Excited state geometry optimisations were performed at the ADC(2)/aug-cc-pVDZ level starting from the S_1, S_2, T_1 and T_2 states for all molecules. In the case of both carboxylic acids, all optimisations converged to minimum energy structures with a deformed –COOH group where the orbital hybridisation changes from the planar sp^2 to tetrahedral sp^3. This is accompanied by an increase in the C–O bond lengths, but also in a shortening of the C_1–C_2 bond and a slight increase in the C_2–C_3 bond length. For the two sulfonic acids, optimisations from each state resulted in dissociation of the sulfo group, indicating that the molecules have no stable excited state minima.

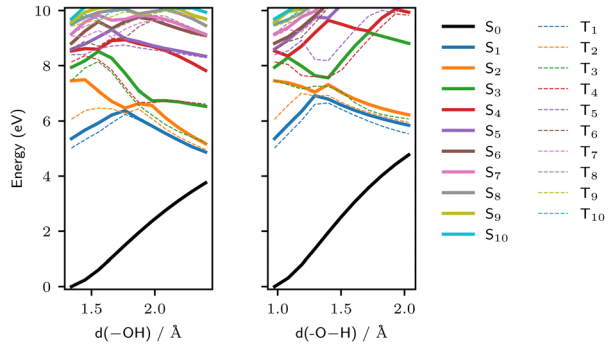

Fig. 2 Scan of the PES of PFBA along the H and OH dissociation coordinates at the RI-ADC(2)/aug-cc-pVDZ level relaxed on the S_0 surface. The ten lowest singlet (full lines) and triplet (dashed lines) excited states are shown.

Next, we look at potential energy surface cuts along the possible dissociation pathways. Looking first at the dissociation curves optimized on the S_0 surface of PFBA (Fig. 2 and 3), we see that dissociation of the –OH group and the fluorine atoms closest to the functional group are energetically favorable both from the singlet and the triplet manifold. On the other hand, dissociation of the C–C bond appears unlikely in the singlet manifold. However, this pathway becomes significantly easier in the triplet manifold where one state is quickly stabilised along the pathway and the barrier along the T_1 state is even lower than the one for –OH dissociation. Results for analogous scans of PFOA are nearly identical (Fig. S6, ESI†).

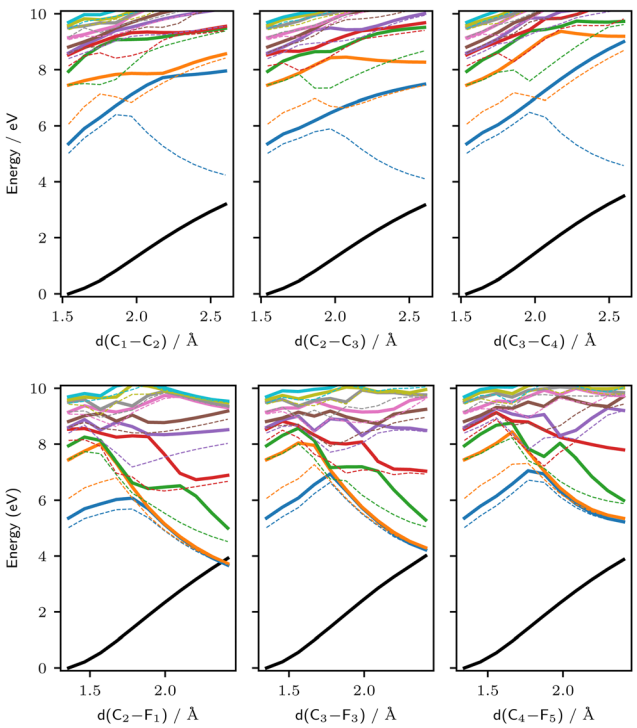

Fig. 3 Scan of the PES of PFBA along the C_1–C_2, C_2–C_3, C_3–C_4, C_2–F_1, C_3–F_3 and C_4–F_5 dissociation coordinates at the RI-ADC(2)/aug-cc-pVDZ level relaxed on the S_0 surface. See Fig. 2 for the legend.

Table 3 Barrier heights along different scans (relaxed on the S_0, S_1 and T_1 potential energy surfaces) of PFBA. The given energies (in eV) can be considered upper bounds on the threshold energies at which certain fragments can start appearing once the molecule is excited

Scan	State	–OH	–H	C_1–C_2	C_2–C_3	C_3–C_4	C_2–F_1	C_3–F_3
S_0	S_1	6.38	6.92	—	—	—	5.69	5.75
S_0	T_1	6.24	6.66	6.40	5.90	6.48	5.34	5.41
S_1	S_1	4.52	5.21	5.12	5.51	—	4.82	5.64
T_1	T_1	4.27	5.16	4.34	4.76	6.24	4.67	5.42

Relaxing the scans on excited state surfaces instead of on the ground state surface results, as expected, in curves with significantly lower barriers (Table 3). In these cuts, all barriers are shown to be below the vertical excitation energy, proving that all dissociation paths are feasible after electronic excitation of the molecules. However, many of the scans relaxed on the excited state surfaces, most notably the C–C bond dissociations, involve larger structural rearrangements. In these scans, the molecule is trapped in a local minimum until the bond is significantly extended at which point a large rearrangement of the molecular backbone occurs and the potential energy drops suddenly. While these pathways are open energetically, the large structural changes involved in the process suggest that they would be less likely than the more direct dissociations due to entropy considerations.

In summary, from these static calculations it is not possible to give an accurate estimate of the branching ratios for PFBA and PFOA where many pathways are open and there is no clear indication that any one of these would dominate. This is especially true for the higher lying excited states where nonadiabatic effects are more important.

For the sulfonic acids (Fig. 4, and Fig. S8 and S9, ESI†) we see that dissociation of the sulfo group is energetically the most favourable pathway, as expected from the unconstrained optimizations. However, we also see that the dissociation curve for the OH group is not very different, making it another likely option. All other pathways for the sulfonic acids appear significantly less probable at low energies. Again, there do not appear to be any significant differences between PFBS and PFOS.

Altogether, upon electronic excitation even to the lowest excited states these molecules will have more than enough energy to access multiple deactivation pathways which are likely to occur on a femtosecond time scale. However, for a quantitative description of the deactivation pathways, nonadiabatic dynamics simulations would need to be performed to account for the coupling between excited states.

3.3 *R*-Matrix scattering calculations

The elastic cross sections for PFBA, PFOA and for PFBS, PFOS are shown in Fig. 5 and 6, respectively. The inelastic cross sections for all four molecules are plotted in Fig. 8.

We present results for scattering energies up to 20 eV for which the continuum basis is sufficiently reliable. Presenting results for energies higher than 20 eV would be in principle

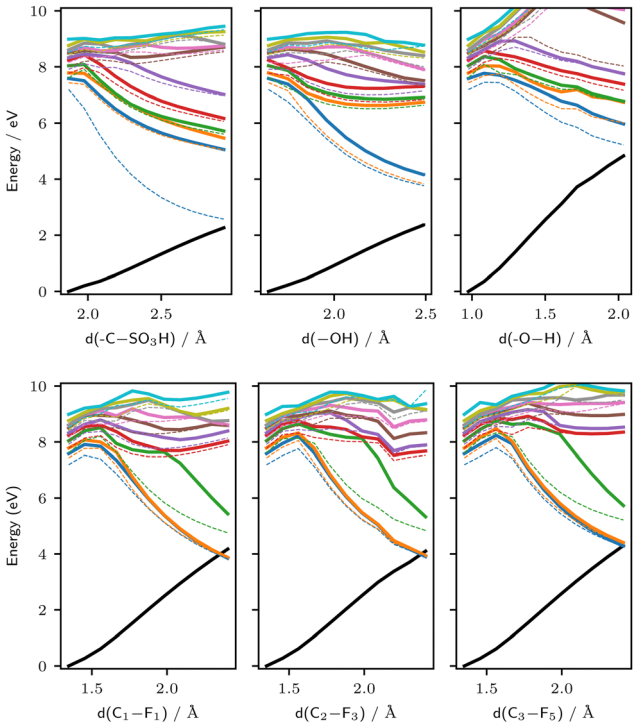

Fig. 4 Scan of the PES of PFBS along the sulfo, OH, H, C_1–F_1, C_2–F_3 and C_3–F_5 dissociation coordinates at the RI-ADC(2)/aug-cc-pVDZ level relaxed on the S_0 surface. See Fig. 2 for the legend.

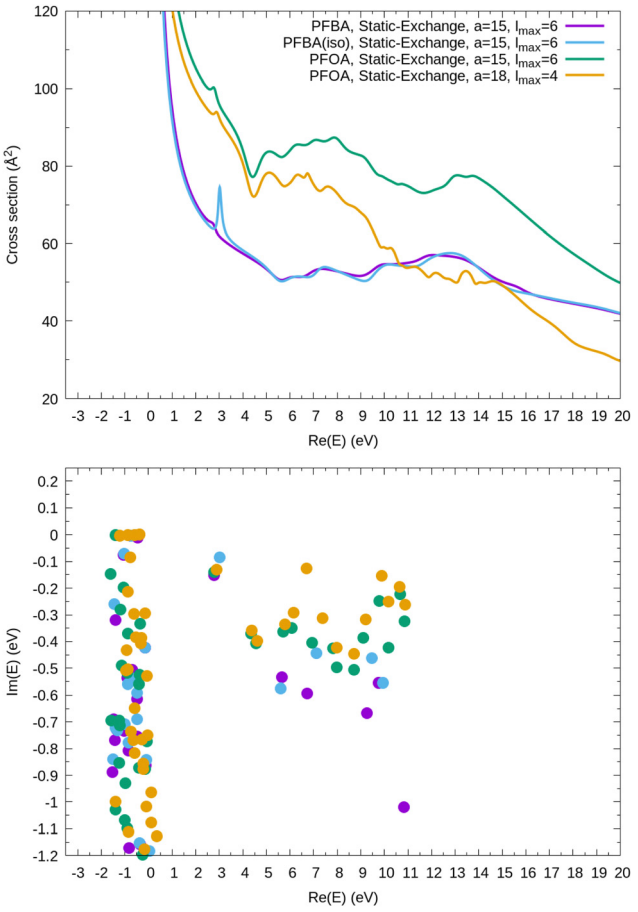

Fig. 5 Elastic scattering cross sections and Siegert (Resonant) states in PFBA and PFOA. Also shown is the result for the second (iso) form of PFBA. Indicated in the legend is the maximum continuum partial wave l_{max} included in each calculation.

possible (even with the GTO-only continuum basis) but our calculations suffer from lack of convergence of the continuum partial wave expansion. Therefore we deem data beyond 20 eV significantly inaccurate and not converged with respect to continuum angular momentum. This is true even for the results with l_{max} = 6 and it is evident from the comparison for PFOA between the calculations with l_{max} = 4 and l_{max} = 6, shown in Fig. 5. The lack of partial wave convergence is especially severe in case of the PFOS molecule, see Fig. 6, where its elastic cross section drops down below that of PFBS at 9 eV. The lack of convergence of the Siegert states for energies above approx. 11 eV is evident even in the calculations with l_{max} = 6. Our tests show that the angular momentum convergence is poor not only due to the polar character of the molecules but mostly due to their geometric size which makes scattering at distances relatively far away from the center of mass still appreciable.

Nevertheless, given the large computational demands of the integral calculations we regard our chosen combination of atomic and continuum bases as sufficient to obtain realistic values for the inelastic cross sections and estimates of the positions and widths of the shape resonances. Both of these are less sensitive to convergence of the partial-wave expansion compared to the elastic cross sections.

3.3.1 Static-exchange results. The SE calculations were performed for a dense grid of energies and were used to obtain basic information about the shape resonances in the system. For resonance analysis we used our newly developed siegert code[11] and applied it to a rectangular grid of 3500 × 3500 complex momenta between the origin and the point k = 0.9–0.35i, *i.e.* up to real energies of approximately 11 eV. The elastic cross sections and the Siegert states are shown on Fig. 5 and 6. Siegert states close to the real axis of momentum correspond to shape resonances and we see that there are many of them in each molecule. Only those Siegert states close to the positive side of the real energy axis are relevant, *i.e.* disregarding the vertical strip of states around Re(E) ≈ 0 eV. While the cross sections suggest presence of resonances at even higher energies beyond 11 eV our results are not sufficiently well converged in angular momentum to give reasonable resonance parameters in the higher energy range. Therefore we didn't perform the resonance search at higher energies. Fig. 5 includes the results for Perfluoroisobutyric acid which is another isomer of PFBA, see Fig. 7. It has the functional group positioned in the middle of the molecule. Our results show that the elastic cross sections for both isomers are very similar: the most striking difference is the width of the lowest-lying shape resonance which can therefore be associated with this functional group. We can speculate that it originates in the π* resonance of the carboxyl group, *i.e.* as in formic acid.[23] On the basis of these results we would expect to see a similar general sensitivity of the cross sections

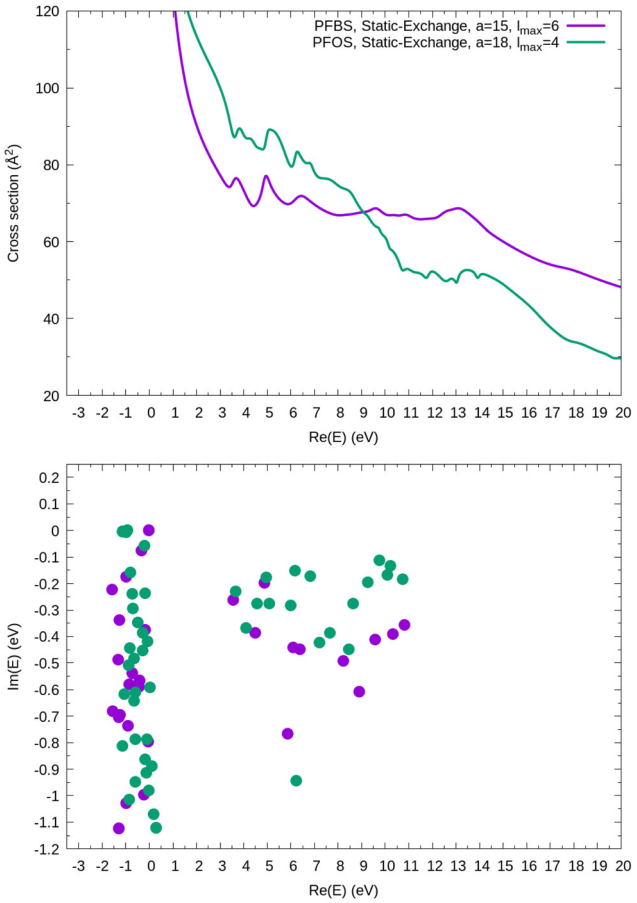

Fig. 6 Elastic scattering cross sections and Siegert (Resonant) states in PFBS and PFOS. Indicated in the legend is the maximum continuum partial wave l_{max} included in each calculation.

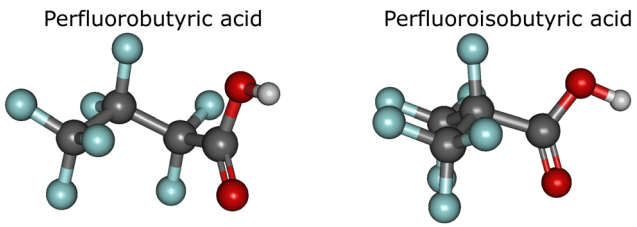

Fig. 7 PFBA isomers. Left: Heptafluorobutyric acid, right: perfluorobutyric acid. The molecule on the left is the one studied in this work.

and resonances to isomerisation also in the other, larger compounds.

The SE calculations represent the first quantitative estimate of elastic cross sections for these large molecules. Nevertheless, all the molecules are polar which implies the need to include higher partial waves in the calculation. This is commonly done by estimating their contribution using the Born approximation[24,25] which can enhance the elastic cross section by an order of magnitude.[26] However, the goal of the present calculations is not to present accurate magnitudes of elastic cross sections but to identify shape resonances which can further enhance the dissociative processes: for this purpose the SE model is sufficient. While this model does not include correlation/polarization effects and therefore overestimates resonance positions[25] it is a well defined reference model which can be used for comparisons against different approaches. To provide an estimate of the resonant shifts we performed exploratory SE calculations for a related molecule, perfluoroisobutyronitrile,[9] for which experimental positions of the lowest-lying resonances are known.[27] We have found that the resonances from the SE model would have to be shifted by at least 2 eV to match the positions of the corresponding lowest-lying resonances in the experiment. On the basis of this analogy we estimate that the SE resonance positions in the PFAS molecules would have to be shifted down by at least the same amount. Additionally, the shift is not linear and a larger shift would be required for the higher-lying resonances. We conclude tentatively that the resonant positions from the SE model are approx. 2–5 eV higher than in experiment.

3.3.2 Complete active space results. To run the CAS calculations a choice of the active space has to be made. The active space for each molecule was chosen on the basis of TDDFT calculations for the seven lowest singlet excited states: the HF orbitals most resembling those of the dominant NTOs for the lowest excited states at the TDDFT level were included in the active space. Table 4 shows the number of "closed" and "occupied" orbitals, used on input for CASSCF calculations in Molpro. The state averaging included, in all cases, 8 singlet and 8 triplet neutral states. The same orbitals and CAS were then employed in the *R*-matrix calculations.

The CAS states were ordered in energy and a total of 25 lowest-lying states of both singlet and triplet character, including the ground state, were employed in the CAS scattering calculations. The results for the 5 lowest-lying CASSCF states are shown in Fig. 8. The complete set of *R*-matrix results is plotted in Fig. S11 (ESI†).

The inelastic cross sections contain many structures which is a complexity to be fully expected for molecules of this size.[26,28] Some of them are associated with the shape resonances but core-excited and Feshbach resonances are expected to be formed too[29] although we have made no attempt to rigorously characterize the peaks also in the view of the limited accuracy of the *R*-matrix calculations. Some of the peaks at energies exceeding the energy of the highest included state will be unphysical pseudoresonances, a typical feature of close-coupling calculations.[25]

In case of the sulfo-containing molecules PFBS and PFOS the cross sections for the various transitions have a comparable

Table 4 Complete active spaces chosen for each molecule in the Molpro nomenclature. The maximum number of CSFs generated for any spin-space symmetry is shown in the last column

	Closed	Occupied	Max. CSFs
PFBA	48	56	2352
PFOA	97	103	189
PFBS	68	76	1512
PFOS	117	125	2352

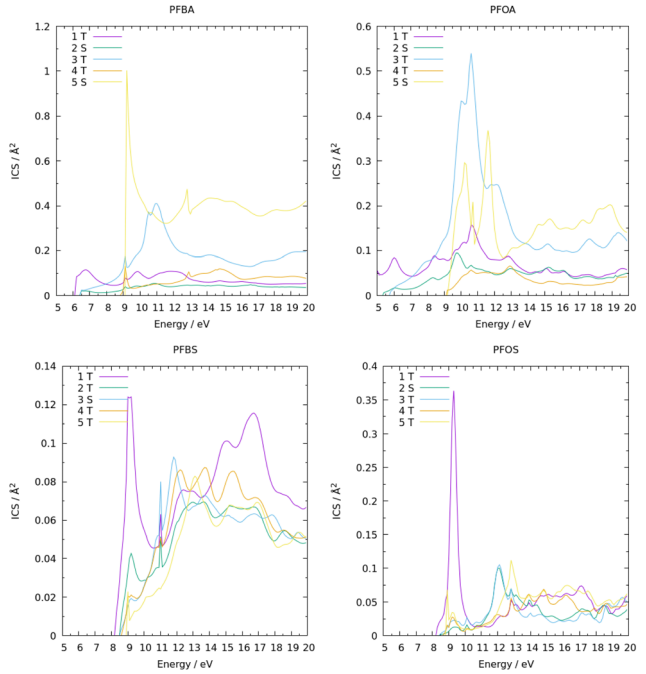

Fig. 8 *R*-Matrix CAS inelastic cross sections for PFBA, PFOA (top row), PFBS, PFOS (bottom row). For clarity results only for the lowest 5 states calculated on the CAS level are shown.

magnitude, while for PFBA and PFOA there are a few dominant transitions. This trend is consistently confirmed by the Born calculations, see below.

3.4 Born calculations for inelastic cross sections

Cross sections for the inelastic scattering for excitations into the 20 lowest singlet excited states at the ADC(2)/aug-cc-pVDZ level were calculated using the Born approximation for PFBA and PFOA (Fig. 9) and for PFBS and PFOS (Fig. 10). As with the previous calculations, we see immediately that the results are mostly dependent on the functional group. In the case of PFBA and PFOA, the S_3 ($\pi\pi^*$) state has the largest cross section, followed by the S_2 ($n\sigma^*$) state. This ordering of the cross-sections was to be expected based on the oscillator strengths of the states since these two values would be directly connected in the dipole Born approximation.[9] In the full Born approximation higher-order terms are included, but the dipole term is still dominant for these molecules and thus we see a strong

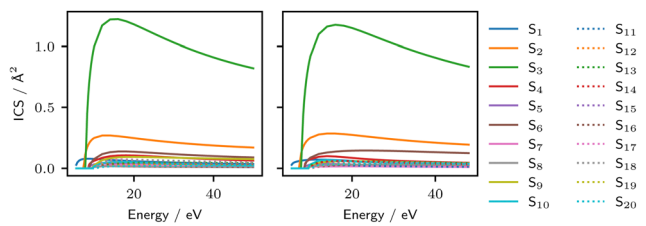

Fig. 9 Inelastic cross sections for excitation into the lowest 20 singlet excited states of PFBA (left) and PFOA (right) calculated at the ADC(2)/aug-cc-pVDZ level using the Born approximation.

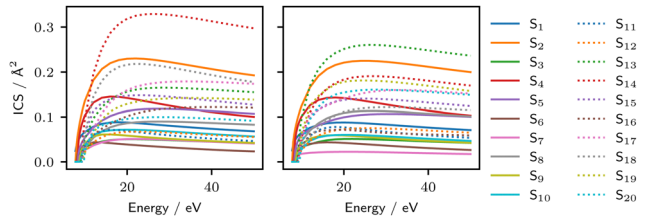

Fig. 10 Inelastic cross sections for excitation into the lowest 20 singlet excited states of PFBS (left) and PFOS (right) calculated at the ADC(2)/aug-cc-pVDZ level using the Born approximation.

correlation between the oscillator strength and cross section. In the case of PFBS and PFOS, the relative cross sections of the different states are much closer.

Fig. 11 shows a comparison between the cross sections calculated for PFBA using the two methods (Born and *R*-matrix) but with the same electronic structure description (CAS). The purpose of this figure is to show the impact of the structured continuum on the cross sections: the role of resonances, state coupling, correlation and electron exchange which are all the effects omitted on the Born level. Despite its simplicity the Born cross sections have a similar magnitude as the *R*-matrix ones. In some cases and energy ranges the results differ from each other by more than 100% but at higher energies approaching 20 eV the magnitude of the *R*-matrix and Born cross sections becomes similar. Nevertheless, for reasons explained above neither of the methods can be regarded as an accurate reference result that we could use to rescale results from the other method. For that reason we can provide only a tentative educated guess to estimate the actual uncertainty of the recommended cross sections to be in the range 50–100%.

On the other hand, the differences in the Born cross sections between Fig. 9 and 11 are exclusively due to the different description of the excited states of PFBA at the ADC(2)/aug-cc-pVDZ and CASSCF/cc-pVDZ levels. While these two results appear significantly different at first glance, the main feature seen in both cases originates from the same $\pi\pi^*$ transition.

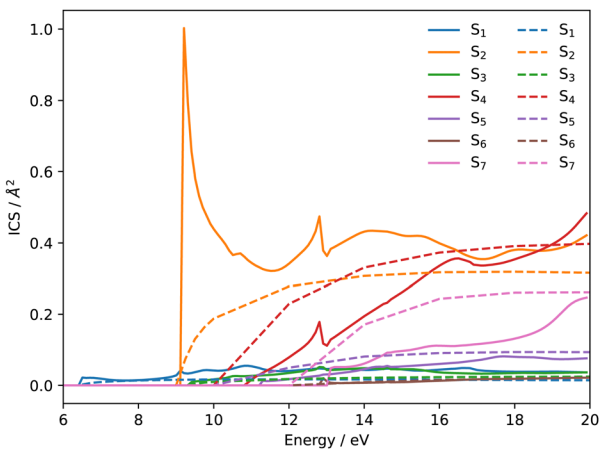

Fig. 11 Comparison of the *R*-matrix (solid lines) and Born (dashed lines) inleastic cross sections for PFBA for the seven lowest-lying singlets in the energy range up to 20 eV.

In the ADC(2) calculation, this transition is mixed with the nRyd(s) transition to form the S_2 and S_3 states, with the S_3 state having the greater involvement of the $\pi\pi^*$ transition and thus having a significantly higher cross section. These same transitions are present at the CASSCF level as states S_2 and S_4, but here the transitions are split almost evenly between the two states and thus the cross sections of the two states are similar.

3.5 Recommended data set for plasma modelling

To estimate cross sections with high accuracy, one needs accuracy both in the electronic structure calculation for target states and in the scattering calculation for the cross sections. As noted in the sections above, the computational cost is prohibitive for quantitative results for molecules of this size so compromises are needed. The Born cross sections calculated on the ADC(2) level are systematically larger than the *R*-matrix derived cross sections. This is in line with our previous experience with the Born approximation. In our previous study[9] we used only the *relative magnitudes* of the Born cross sections since those are needed to initiate simulations of the nuclear dynamics following electron impact. In this case however we require *absolute* cross sections. Comparing the Born and the *R*-matrix CAS cross sections, *cf.* Fig. 8–10, we see that the Born cross sections are good at reproducing the overall trends in the cross sections: PFBA and PFOA have a few dominant singlet states while magnitudes of the PFBS and PFOS cross sections are more uniform. The relative magnitudes for the pair PFBA, PFOA *vs.* PFBS, PFOS are also consistent with *R*-matrix results. Therefore the final data set comprises the following cross sections:

- Born cross sections for impact excitation of the singlet states for the energy range 0–50 eV from Fig. 9 and 10.
- *R*-matrix cross sections for impact excitation of the triplet states for the energy range 0–20 eV from Fig. 8.

The full set of our recommended inelastic cross sections for all molecules is plotted in Fig. S10 (ESI†). The advantage of the Born singlet cross sections lies in much more accurate threshold energies: the CAS thresholds cannot be trusted beyond the first few lowest-lying states, *cf.* Tables 1 and 2. Additionally, the Born cross sections don't suffer from angular momentum convergence issues, particularly at higher impact energies. This is due to the momentum-space formulation of the Born calculation. On the other hand the singlet Born cross sections miss all features associated with the many shape resonances and background scattering, *i.e.* structured continuum. It can be expected that the *R*-matrix triplet excitation cross sections would be less sensitive to lack of angular momentum convergence since the transition dipole is zero: the excitation process is not dominated by the long-range dipole interaction as is the case for the singlet–singlet transitions but by electron exchange and correlation.

The recommended excitation cross sections shown in Fig. S10 (ESI†) can be summed to estimate the cross sections for dissociative excitation into triplet and singlet states. This estimation was done on the assumption that the excited levels are dissociative which is further justified by the repulsive PES scans for the corresponding dissociative coordinates shown in Fig. 2–4. In the plasma modelling, we used the 20 separate singlet cross sections and the 12 or 13 separate triplet cross sections computed, as opposed to the sum of the singlet and triplet cross sections. In addition, the ionization cross sections were also computed *via* the binary encounter Bethe[30] model which is conveniently implemented in Quantemol's electron scattering (QEC) interface.[31]

3.6 Modelling PFAS degradation in a plasma

To demonstrate the utility of the fundamental cross sections described in Section 3.5, the cross sections were implemented in *GlobalKin*, a 0-dimensional plasma chemistry model, and were used to model the decomposition of PFBA, PFOA, PFBS, and PFOS in an atmospheric pressure plasma. *GlobalKin* is described in detail in Lietz and Kushner[32] and will be only briefly described here. The continuity equations for each chemical species are integrated, including sources and losses due to electron impact, ion and neutral chemical reactions, flow, and diffusion to the bounding surfaces of the plasma. The electron temperature and gas temperature are calculated using their respective energy conservation equations. In an atmospheric pressure plasma, the electron temperature is typically a few eV, while the gas temperature is close to room temperature. While the rate coefficients of heavy species reactions are specified in Arrhenius form, the rates of electron impact processes are based on rate coefficients derived from the electron energy distribution, calculated by solving Boltzmann's equation. The solution of Boltzmann's equation generates a look-up table of electron impact rate coefficients for different electron temperatures. The look-up table is periodically updated during the simulation.

The decomposition of PFBA, PFOA, PFBS, and PFOS was examined in a repetitively pulsed Ar plasma at atmospheric pressure in a configuration corresponding to a dielectric barrier discharge. Plasmas containing each PFAS molecule were examined individually (Ar/PFBA, Ar/PFOA, Ar/PFBS, and Ar/PFOS) with the ratio Ar/PFAS = 99.5/0.5. The species in the reaction mechanism include Ar, H_2O, O_2, CO_2, F_2, C_xF_y ($x \leq 3$), HSO_3, and their dissociation fragments and radicals, excited states, and ions. The $Ar/H_2O/O_2$ reaction mechanism is based on Van Gaens and Bogaerts,[33] and the fluorocarbon mechanism is from Vasenkov *et al.*[34] The PFAS species and their dissociation products, including C_xF_y ($x \geq 4$), were added to the mechanism.

The decomposition reactions of the PFAS molecules are listed in Table 5. The mechanism includes dissociative ionization (DI), charge-exchange (CEX), dissociative attachment (DA), and dissociative excitation transfer (DET) from Ar excited states. Note that only ions with an ionization potential greater than the PFAS ionization potentials can participate in CEX reactions. (PFAS ionization potentials were taken from Wiens *et al.*[8]) The DA rate coefficients reported in Wiens *et al.*[8] are thermally attaching rate coefficients, neglecting resonances at higher electron energies. The rates of DET were estimated from rates of DET with other fluorocarbons.[34] The cross sections

Table 5 Decomposition reactions for PFBA, PFOA, PFBS, and PFOS included in the plasma simulations. $M^+ = Ar^+, Ar_2^+$ (neutral products are Ar and Ar), H^+, H_2^+, H_3^+ (neutral products are H_2 and H), OH^+, O_2^+, O_4^+ (neutral products are O_2 and O_2), $O^+, CO^+, CO_2^+, F_2^+, F^+, CF_2^+, C_2F_2^+$, and C_2F^+. Ar* = Ar($1s_1$), Ar($1s_2$), Ar($1s_3$), Ar($1s_4$), Ar(4P), Ar(4D)

Dissociative excitation to singlet states	$e + PFBA \rightarrow C_3F_7CO + OH + e$	This work
	$e + PFOA \rightarrow C_7F_{15}CO + OH + e$	This work
	$e + PFBS \rightarrow HSO_3 + C_4F_9 + e$	This work
	$e + PFOS \rightarrow HSO_3 + C_8F_{17} + e$	This work
Dissociative excitation to triplet states	$e + PFBA \rightarrow C_2F_4 + TFA + e$	This work
	$e + PFOA \rightarrow C_6F_{12} + TFA + e$	This work
	$e + PFBS \rightarrow HSO_3 + C_4F_9 + e$	This work
	$e + PFOS \rightarrow HSO_3 + C_8F_{17} + e$	This work
Dissociative ionization (DI)	$e + PFBA \rightarrow C_2F_4^+ + TFA + e$	Binary encounter Bethe
	$e + PFOA \rightarrow C_2F_4^+ + PFHxA + e$	Binary encounter Bethe
	$e + PFBS \rightarrow C_2F_4^+ + PFES + e$	Binary encounter Bethe
	$e + PFOS \rightarrow C_2F_4^+ + PFHxS + e$	Binary encounter Bethe
Charge-exchange (CEX)	$M^+ + PFBA \rightarrow HCOO^+ + C_3F_7 + M$	8
	$M^+ + PFOA \rightarrow C_3F_5^+ + CO_2 + HF + C_4F_9 + M$	8
	$M^+ + PFBS \rightarrow C_2F_5^+ + C_2F_4 + HSO_3 + M$	Assumed from PFBA[8]
	$M^+ + PFOS \rightarrow C_3F_5^+ + C_5F_{12} + HSO_3 + M$	Assumed from PFOA[8]
Dissociative attachment (DA)	$e + PFBA \rightarrow C_3F_6HCOO^- + F$	H–F elimination[8]
	$e + PFOA \rightarrow C_7F_{14}HCOO^- + F$	H–F elimination[8]
	$e + PFBS \rightarrow C_4F_9SO_3^- + H$	Assumed from PFBA[8]
	$e + PFOS \rightarrow C_8F_{17}SO_3^- + H$	Assumed from PFOA[8]
Dissociative excitation transfer (DET)	$Ar^* + PFBA \rightarrow HCOO^+ + C_3F_7 + Ar + e$	Estimated
	$Ar^* + PFOA \rightarrow C_3F_5^+ + CO_2 + HF + C_4F_9 + Ar + e$	Estimated
	$Ar_2^* + PFOA \rightarrow C_3F_5^+ + CO_2 + HF + C_4F_9 + Ar + Ar + e$	Estimated
	$Ar^* + PFBS \rightarrow C_2F_5^+ + C_2F_4 + HSO_3 + Ar + e$	Estimated
	$Ar^* + PFOS \rightarrow C_3F_5^+ + C_5F_{12} + HSO_3 + Ar + e$	Estimated
	$Ar_2^* + PFOS \rightarrow C_3F_5^+ + C_5F_{12} + HSO_3 + Ar + Ar + e$	Estimated

from Section 3.5 were implemented in *GlobalKin* allowing for electron impact dissociative excitation to singlet or triplet states. Note that each individual singlet or triplet cross section was used for the plasma modelling. For the carboxylic acids (PFBA, PFOA), excitation to singlet states removes an OH from the acid head group, while excitation to triplet states breaks the C–C chain, forming a shorter-chain PFAS molecule (TFA) and a fluoroalkane. For the sulfonic acids (PFBS, PFOS), excitation to either the singlet or triplet states removes the HSO_3 acid group. Further study is needed to determine the precise products of dissociation from each individual singlet and triplet state. The reaction mechanism was constructed to decrease the C–C chain in the PFAS molecules by 2 C atoms at a time. Therefore, all reactions that occur for PFBA, PFOA, PFBS, and PFOS are assumed to occur with the same rate coefficient or cross section for TFA, PFHxA, PFES, and PFHxS, respectively. While VUV photons could degrade the PFAS molecules,[35] they were not included in the present reaction mechanism. However, we expect the inclusion of these reactions would only increase the rate of degradation of the PFAS molecules. As many of the rates and products of the PFAS decomposition reactions are estimated, the results of *GlobalKin* should be regarded as qualitative.

The decomposition of the PFAS molecules was examined in a pulsed nanosecond dielectric barrier discharge operating at atmospheric pressure. The power pulse ramps up for 15 ns and stays constant to 82 ns. The power then decreases to 1% of the peak value at 115 ns. 5.8 mJ cm^{-3} is deposited in the plasma for each pulse, and the peak power deposition is 68 kW cm^{-3}. The pulse repetition frequency is 10 kHz, corresponding to a pulse every 0.1 ms. The evolution of the plasma is tracked over 20 pulses.

As shown in Fig. 12a for Ar/PFOA, the electron density rapidly increases as the power ramps up. The reactivity in the plasma is driven by the hot electrons either directly through electron impact processes or indirectly through the formation of positive ions and excited states that react with the PFAS molecules through CEX or DET. While the electron temperature ranges from 4–5 eV (average electron energy of 6–7.5 eV), the electrons in the tail of the energy distribution have energies above the thresholds for electron impact processes with Ar and PFAS molecules. While the plasma remains quasi-neutral, the dominant negative charge becomes the negative ions within the first 2 ns as DA with the PFAS molecules forms negative ions. During the plasma pulse, the positive and negative ion densities are over an order of magnitude larger than the electron density, and the electron temperature is around 4 eV. As the power decreases, the electron density decreases rapidly due to DA and recombination with positive ions. The positive and negative ion densities decrease over a longer timescale, as the dominant consumption mechanism is ion–ion neutralization which proceeds at heavy particle rates (as opposed to electron

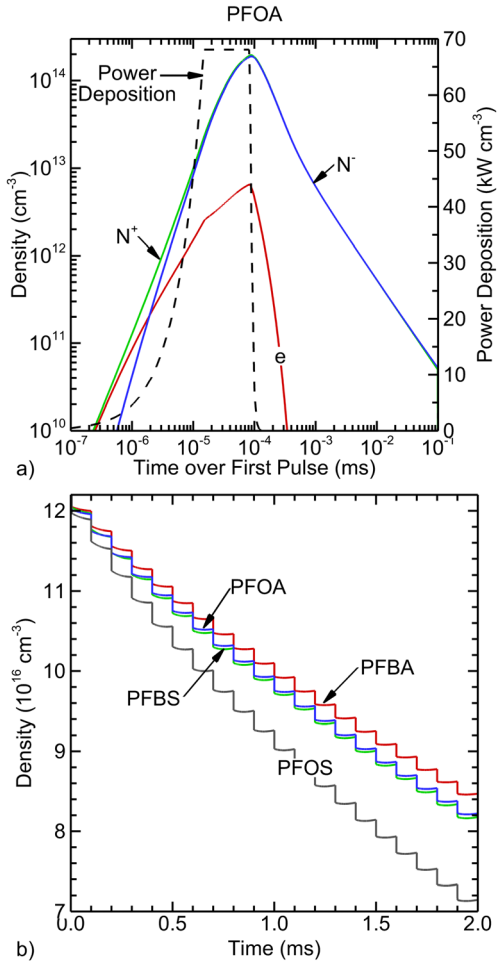

Fig. 12 (a) Electron, positive ion, and negative ion densities in the Ar/PFOA plasma over the first pulse. (b) Decomposition of PFBA, PFOA, PFBS, and PFOS over 20 pulses.

rates). The plasma properties, and in particular the electron density depend on the PFAS molecule. The electron density is lower for Ar/PFBA and Ar/PFBS (7–8 $\times$ 10^{11} cm^{-3}) than Ar/PFOA (7 $\times$ 10^{12} cm^{-3}) at the time the power begins to ramp down, while the electron density is higher for Ar/PFOS (10^{13} cm^{-3}) than Ar/PFOA. However, the positive and negative ion densities are less affected by the PFAS molecule, ranging from 1.9 $\times$ 10^{14} cm^{-3} for Ar/PFOA to 2.5 $\times$ 10^{14} cm^{-3} for Ar/PFOS.

The decomposition of PFBA, PFOA, PFBS, and PFOS over 20 pulses is shown in Fig. 12(b). The initial concentrations of the PFAS molecules are 1.2 $\times$ 10^{17} cm^{-3}. Most of the PFAS degradation occurs during the plasma pulse as the species that react with the PFAS molecules (electrons, positive ions, and excited states) are most prevalent during the pulse. There are few reactions between pulses that decompose the PFAS molecules. PFOS exhibits the largest degradation, reaching 7.2 $\times$ 10^{16} cm^{-3} (40% of PFOS degraded) at 2 ms. PFBA has the lowest degradation, reaching 8.5 $\times$ 10^{16} cm^{-3} (30% of PFBA degraded) at 2 ms. Two trends can be identified: the sulfonic acids (PFBS, PFOS) decompose at faster rates than the carboxylic acids (PFBA, PFOA), and the long-chain compounds (PFOA, PFOS) decompose at faster rates than the short-chain compounds (PFBA, PFBS). These trends have been observed in previous work on plasma degradation of PFAS molecules. PFOS has been observed to decompose at a faster rate than PFOA,[17] and short-chain compounds have been shown to decompose at slower rates than long-chain compounds.[12] While these studies were performed with PFAS molecules solvated in water, the results for gas phase decomposition presented here reproduce the observed trends.

The roles of the different processes listed in Table 5 in degrading the PFAS compounds were examined. The rates of these processes are shown in Fig. 13 over the first pulse for PFBA, PFOA, PFBS, and PFOS. While the rates of DA are similar for all of the PFAS molecules, the rates of other decomposition reactions change depending on the PFAS molecule. CEX has a higher rate for the short-chain molecules than for the long-chain molecules. The short-chain species have higher concentrations of the species able to participate in CEX reactions. DI has higher rates for the sulfonic acids than for the carboxylic acids due in part to lower threshold energies for the sulfonic acids. DET occurs at higher rates for the long-chain species, driven by the additional DET reaction with Ar_2^* for the long-chain species compared to the short-chain species. Dissociative excitation to singlet and triplet states occurs at a higher rate in the long-chain *versus* the short-chain species, driven by an increased electron density in the long-chain cases.

To explicitly demonstrate the effect of the dissociative excitation to singlet and triplet states, these processes were removed from the model. The resulting degradation percentages decreased by less than 5% of the initial PFAS molecule,

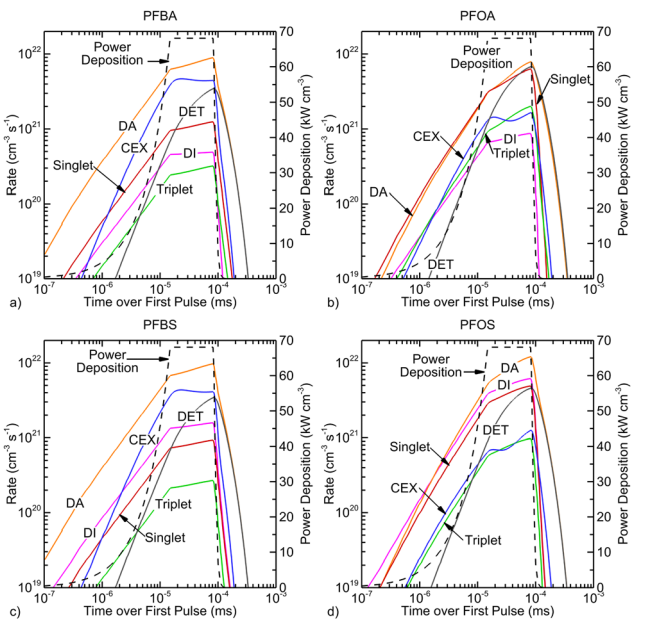

Fig. 13 Rates of decomposition over the first pulse of (a) PFBA, (b) PFOA, (c) PFBS, and (d) PFOS. Decomposition occurs by dissociative excitation to singlet and triplet states, dissociative attachment (DA), charge-exchange (CEX), dissociative ionization (DI), and dissociative excitation transfer (DET) from Ar excited states.

with the largest difference seen for PFOA. When removing the dissociative excitation to singlet and triplet states, the rates of the other degradation reactions do not remain constant; instead, they increase. CEX and DET play a larger role as the densities of the ions and Ar excited states increase when dissociative excitation reactions are removed. The rates of DA and DI also increase when dissociative excitation reactions are removed as the electron density increases. This is more prominent in the long-chain species compared to the short-chain species.

Finally, the carbon containing products of the PFAS decomposition were assessed. The products, grouped by number of C atoms they contain, are shown in Fig. 14. For Ar/PFBA (Fig. 14(a)), species with 1, 3, and 4 C atoms dominate. The dominant C compound is CO, formed from spontaneous decomposition of the radical $C_3F_7CO \rightarrow C_3F_7 + CO$[36] and electron recombination with $HCOO^+$. The dominant C_3 compound is C_3F_7, formed from decomposition of C_3F_7CO and a direct product of CEX with PFBA. The dominant C_4 compound is C_3F_6 HCOO, a H–F elimination product formed from ion–ion neutralization of the DA product $C_3F_6HCOO^-$. Note that C_3F_6HCOO is a terminal species in the mechanism. For Ar/PFOA (Fig. 14(b)), the C products dominate. The 2 most prevalent C products are CO_2, formed from DET and electron recombination with $HCOO^+$, and CO, from spontaneous decomposition of $C_7F_{15}CO$ and electron recombination with $HCOO^+$. For Ar/PFBS (Fig. 14c), 1, 2, and 4 C atom species are the dominant products. The dominant C_2 product is C_2F_3, formed by dissociative ion–ion neutralization of $C_4F_9SO_3^-$ and $C_2F_5^+$. $C_2F_5^+$ is formed directly through CEX or DET with PFBS. The dominant C_4 product is C_4F_9, formed directly through dissociative electron impact excitation to singlet and triplet states and through ion–ion neutralization of $C_4F_9SO_3^-$. Note that C_4F_9 is a terminal species in this mechanism. The dominant C product is CF_4, formed from three-body recombination of CF_3 and F. CF_3 is formed from ion–ion neutralization of $C_4F_9SO_3^-$ and $C_2F_5^+$. For Ar/PFOS (Fig. 14(d)), the C_8 species have the largest concentration. The dominant C_8 product is C_8F_{17}, formed directly from dissociative electron impact excitation to singlet and triplet states as well as dissociative ion–ion recombination of $C_8F_{17}SO_3^-$. Note that C_8F_{17} is a radical, but in this mechanism, it is a terminal species as reactions and their corresponding rate coefficients with other species are not known.

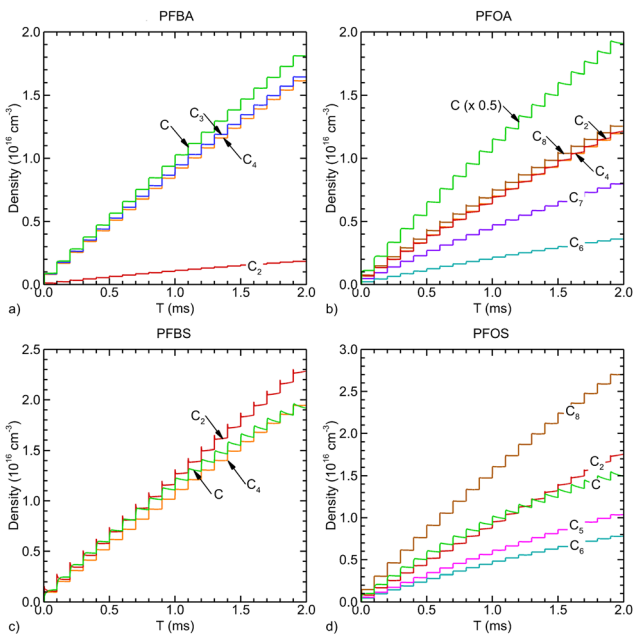

Fig. 14 Carbon containing decomposition products for (a) PFBA, (b) PFOA, (c) PFBS, and (d) PFOS. Products are grouped by the number of C atoms they contain.

4 Discussion

The purpose of this work was to elucidate the role of electron impact processes in plasma degradation of PFAS molecules in the gas phase. Electron-induced processes were found to be dominant with the largest contribution from DA in all molecules. In PFOA and PFOS the role of DET is comparable to the DA.

The role of DA however is expected to be even more important since our mechanism includes only the DA rates from Wiens *et al.*[8] which cites values only up to temperatures of 600 K while ideally, we would require DA cross sections up to 10–15 eV of electron energy which are currently not available. Crucially, our electron scattering calculations reveal a large number of shape resonances from near-threshold energies up to approx. 10 eV which are expected to further enhance the contribution of DA through generation of molecular fragments other than neutral F and H which dominate at low energies. The role of resonances can be especially important since the electron temperature in our simulations is 4–5 eV which lies in the middle of the resonant region.

As the plasma degradation takes place in dielectric barrier discharge an increased degradation of PFAS can be expected when VUV photoionduced processes are also included.[35]

The high level challenge that this work aims to contribute to is plasma-based treatment of PFAS-contaminated water. The plasma modelling described here considers only gas phase processes and is a first step towards modelling the more complex plasma–liquid interactions that occur with water containing PFAS molecules. While the results presented in Section 3.6 are based on several assumptions, the results demonstrate the variety of reactive species (electrons, ions, Ar*) that contribute to PFAS decomposition. The PFAS molecules are often preferentially found at the plasma–liquid interface due to their surfactant nature. Reactions between PFAS molecules and gas phase reactive species can occur at the plasma–liquid interface. In particular, the reactions with electrons can occur before the electrons solvate.[6] Once the electrons solvate into the liquid, they react within tens of nm of the interface. The reactions at the interface are particularly sensitive to the surface activity of the PFAS species, determining the concentration of the PFAS

species at the interface. Since long-chain species have larger surface activities than short-chain species, direct electron impact processes and processes involving solvated electrons would contribute to increased rates of degradation of the long-chain species. Other reactions not considered in this work become important in a solvated context, including the proposed decarboxylation–hydroxylation–elimination–hydrolysis (DHEH) process initiated by solvated electrons to shorten the C–C chain in carboxylic acids.[37,38] It has also been observed that PFOS degrades to PFOA, perhaps through the intermediate C_8F_{17}, formed by removal of the sulfonic acid group by solvated electrons, participating in a hydroxylation–elimination–hydrolysis process.[17]

5 Conclusions

We have investigated the role of electron impact processes in plasma degradation of PFAS in a pulsed dielectric barrier discharge. The plasma degradation model included electron impact dissociative excitation, dissociative ionization, and dissociative attachment; and the heavy particle processes of charge-exchange and dissociative excitation transfer.

To provide the data required to model electron impact dissociative excitation we calculated both electron-impact elastic and inelastic cross sections using well-defined models and performed calculations of the likely fragmentation dynamics that would occur following excitation into singlet and triplet states.

The elastic cross sections show that all PFAS molecules investigated here posses a large number of shape resonances spanning near-threshold region up to the ionization potential. The electron impact cross sections are strongly enhanced by these resonances. The role of resonances is expected to be important as the plasma simulations show that electrons responsible for dissociative collisions with PFAS molecules have average energies of 4–5 eV. However, little data on dissociative attachment to PFAS are presently available for this energy region except for the low-energy data derived from the experiments of Wiens *et al.*[8]

The importance of electron impact dissociative excitation varies depending on the molecule. A more detailed assessment of this process will require subsequent calculations of nuclear dynamics including non-adiabatic dynamics and consideration of the environment. In the current work we have performed an extensive exploration of the potential energy surfaces of these molecules and have shown that (1) the computational cost required for a reasonable description of the excited states of the smaller molecules is low enough to allow mixed quantum-classical simulations of the dissociative excitation process, and (2) that the excited state potential energy surfaces of PFOA and PFOS are close enough to those of, respectively, PFBA and PFBS that results for the smaller molecules could be generalized to the larger ones. With such calculations branching ratios (in addition to cross sections) could be provided for plasma modelling which would complete the *ab initio* treatment for dissociative excitation.

Author contributions

MS performed the electronic structure and Born calculations. ZM performed the *R*-matrix calculations. HA generated the dissociative excitation cross sections. MM and MK performed the plasma modelling. All authors contributed to analysis of the results and writing of the manuscript.

Data availability

The final set of recommended electronically inelastic electron collision cross sections as described in Section 3.5 is available at Zenodo at **https://doi.org/10.5281/zenodo.13826246**. Further data supporting this article have been included as part of the ESI.† The UKRmol+ code can be found at Zenodo **https://doi.org/10.5281/zenodo.5799110**. The version of the code employed for this study is version 3.2. The Born calculations were performed with a development branch ''pw_integrals'' available from GitLab: **https://gitlab.com/Ukamor/UKRMol/GBTOLi**.

Conflicts of interest

There are no conflicts to declare.

Acknowledgements

The work of M. Meyer and M. J. Kushner was supported by 3M Company, the US National Science Foundation (CBET-2032604), and US Department of Energy Office of Fusion Energy Sciences (DE-SC0020232). Zdenek Mašín and Marin Sapunar acknowledge the support of the Czech Science Foundation (grant no. 20-15548Y). Quantemol Ltd is acknowledged for initiating this collaboration, providing data for plasma modelling, and for partial support of ZM and MS in this work. MM and MK thank Jisu Jeon for converting raw cross section data for use in the global modeling platform.

Notes and references

1 J. Glüge, M. Scheringer, I. T. Cousins, J. C. DeWitt, G. Goldenman, D. Herzke, R. Lohmann, C. A. Ng, X. Trier and Z. Wang, *Environ. Sci.: Processes Impacts*, 2020, **22**, 2345–2373.
2 E. C. Agency, *Per- and polyfluoroalkyl substances (PFAS)*, **https://echa.europa.eu/hot-topics/perfluoroalkyl-chemicals-pfas**.
3 U. S. E. P. Agency, *Per- and Polyfluoroalkyl Substances*, **https://www.epa.gov/sdwa/and-polyfluoroalkyl-substances-pfas**.
4 D. M. Wanninayake, *J. Environ. Manage.*, 2021, **283**, 111977.
5 D. Palma, C. Richard and M. Minella, *Chem. Eng. J. Adv.*, 2022, **10**, 100253.
6 G. R. Stratton, F. Dai, C. L. Bellona, T. M. Holsen, E. R. V. Dickenson and S. Mededovic Thagard, *Environ. Sci. Technol.*, 2017, **51**, 1643–1648.

7 Y. Deng, Z. Liang, X. Lu, D. Chen, Z. Li and F. Wang, *Chemosphere*, 2021, **283**, 131168.
8 J. P. Wiens, T. M. Miller, S. G. Ard, A. A. Viggiano and N. S. Shuman, *J. Phys. Chem. A*, 2022, **126**, 9076–9086.
9 T. Ovad, M. Sapunar, Š. Sršen, P. Slavíček, Z. Mašín, N. C. Jones, S. V. Hoffmann, M. Ranković and J. Fedor, *J. Chem. Phys.*, 2023, **158**, 014303.
10 Z. Mašín, J. Benda, J. D. Gorfinkiel, A. G. Harvey and J. Tennyson, *Comput. Phys. Commun.*, 2020, **249**, 107092.
11 T. P. Ragesh Kumar, P. Nag, M. Ranković, T. F. M. Luxford, J. Kočišek, Z. Mašín and J. Fedor, *J. Phys. Chem. Lett.*, 2022, **13**, 11136–11142.
12 R. K. Singh, E. Brown, S. Mededovic Thagard and T. M. Holsen, *J. Hazard. Mater.*, 2021, **408**, 124452.
13 H. Zhang, P. Li, A. Zhang, Z. Sun, J. Liu, P. Héroux and Y. Liu, *Environ. Sci. Technol.*, 2021, **55**, 16067–16077.
14 M. J. Johnson, W. A. Maza, V. M. Breslin, D. R. Boris, T. B. Petrova and S. G. Walton, *Plasma Sources Sci. Technol.*, 2022, **31**, 085001.
15 G. Nayak, J. Wang, R. Li, D. Aranzales, S. M. Thagard and P. J. Bruggeman, *Plasma Processes Polym.*, 2023, 1–18.
16 J. R. Groele, N. Sculley, T. M. Olson and J. E. Foster, *J. Appl. Phys.*, 2021, **130**, 053304.
17 R. K. Singh, S. Fernando, S. F. Baygi, N. Multari, S. M. Thagard and T. M. Holsen, *Environ. Sci. Technol.*, 2019, **53**, 2731–2738.
18 S. G. Balasubramani, G. P. Chen, S. Coriani, M. Diedenhofen, M. S. Frank, Y. J. Franzke, F. Furche, R. Grotjahn, M. E. Harding, C. Hättig, A. Hellweg, B. Helmich-Paris, C. Holzer, U. Huniar, M. Kaupp, A. Marefat Khah, S. Karbalaei Khani, T. Müller, F. Mack, B. D. Nguyen, S. M. Parker, E. Perlt, D. Rappoport, K. Reiter, S. Roy, M. Rückert, G. Schmitz, M. Sierka, E. Tapavicza, D. P. Tew, C. Van Wüllen, V. K. Voora, F. Weigend, A. Wodyński and J. M. Yu, *J. Chem. Phys.*, 2020, **152**, 184107.
19 TURBOMOLE V7.6.1 2022, a Development of University of Karlsruhe and Forschungszentrum Karlsruhe GmbH, 1989–2007, TURBOMOLE GmbH, since 2007, Available from **https://www.turbomole.org**.
20 H.-J. Werner and P. J. Knowles, *et al.*, *MOLPRO, a package of ab initio programs*, Stuttgart, Germany, 2012.
21 T. Shiozaki, *Wiley Interdiscip. Rev.: Comput. Mol. Sci.*, 2018, **8**, e1331.
22 A. Faure, J. D. Gorfinkiel, L. A. Morgan and J. Tennyson, *Comput. Phys. Commun.*, 2002, **144**, 224–241.
23 R. Janečková, D. Kubala, O. May, J. Fedor and M. Allan, *Phys. Rev. Lett.*, 2013, **111**, 213201.
24 N. Sanna and F. A. Gianturco, *Comput. Phys. Commun.*, 1998, **114**, 142–167.
25 J. Tennyson, *Phys. Rep.*, 2010, **491**, 29–76.
26 Z. Mašín, J. D. Gorfinkiel, D. B. Jones, S. M. Bellm and M. J. Brunger, *J. Chem. Phys.*, 2012, **136**, 144310.
27 M. Ranković, T. P. R. Kumar, P. Nag, J. Kočišek and J. Fedor, *J. Chem. Phys.*, 2020, **152**, 244304.
28 K. Regeta, M. Allan, Z. Mašín and J. D. Gorfinkiel, *J. Chem. Phys.*, 2016, **144**, 024302.
29 Z. Mašín and J. D. Gorfinkiel, *J. Chem. Phys.*, 2012, **137**, 204312.
30 Y.-K. Kim and M. E. Rudd, *Phys. Rev. A: At., Mol., Opt. Phys.*, 1994, **50**, 3954–3967.
31 B. Cooper, M. Tudorovskaya, S. Mohr, A. O'Hare, M. Hanicinec, A. Dzarasova, J. D. Gorfinkiel, J. Benda, Z. Mašín, A. F. Al-Refaie, P. J. Knowles and J. Tennyson, *Atoms*, 2019, **7**, 97.
32 A. M. Lietz and M. J. Kushner, *J. Phys. D: Appl. Phys.*, 2016, **49**, 425204.
33 W. Van Gaens and A. Bogaerts, *J. Phys. D: Appl. Phys.*, 2013, **46**, 275201.
34 A. V. Vasenkov, X. Li, G. S. Oehrlein and M. J. Kushner, *J. Vac. Sci. Technol., A*, 2004, **22**, 511–530.
35 J. Chen, P. Yi Zhang and J. Liu, *J. Environ. Sci.*, 2007, **19**, 387–390.
36 O. Setokuchi, S. Kutsuna and M. Sato, *Chem. Phys. Lett.*, 2006, **429**, 360–364.
37 M. J. Bentel, Y. Yu, L. Xu, Z. Li, B. M. Wong, Y. Men and J. Liu, *Environ. Sci. Technol.*, 2019, **53**, 3718–3728.
38 J. Cui, P. Gao and Y. Deng, *Environ. Sci. Technol.*, 2020, **54**, 3752–3766.

